Original Article

Electrocatalytic decomposition mechanism of hydroxyamine nitrate on the Cu(111) surface

Men Li[a], Tianpeng Li[a,*], Xinbao Gao[a], Yin Huang[b,*]

[a]National Demonstration Center of Experimental Teaching for Ammunition Support and Safety Evaluation Education, Army Engineering University of PLA, Hebei Shijiazhuang 050000, China
[b]Hubei Institute of Aerospace Chemistry Technology, Hubei Xiangyang 441000, China

ARTICLE INFO

ABSTRACT

Hydroxylamine nitrate (HAN)-based electrically controlled solid propellants are currently the mainstream electrically controlled solid propellants. To gain a deeper understanding of their electrically controlled combustion mechanisms, this study employed quantum chemical simulations to systematically explore the electrocatalytic decomposition of HAN on a Cu(111) surface. The findings indicate that the electrocatalytic decomposition of NO_3^- ions on the anode surface is the dominant reaction for O_2 generation, with a reaction barrier significantly lower than that of water electrolysis, demonstrating a pronounced reaction advantage. By optimizing the configurations of adsorbed molecules during the reaction and calculating the barriers for each reaction step, we have detailed the mechanism of HAN's electrocatalytic decomposition on the Cu(111) surface. Additionally, the reaction on a cathode surface is relatively facile, with the key step being the adsorption and decomposition of NH_3OH^+ ions on the cathode surface. The generation of hydrogen ions in the anode reaction and their consumption in the cathode reaction lead to the cathode solution becoming alkaline and the anode solution becoming acidic after electrolysis. These findings provide important theoretical insights into the electrically controlled combustion mechanisms of HAN-based electrically controlled solid propellants.

1. Introduction

Electrically controlled solid propellants, a new variant that can be ignited, burned, and extinguished using electrical energy control, are attracting widespread attention in the controllable propulsion field [1]. At present, most electrically controlled solid propellants are based on hydroxylamine nitrate (HAN) [2], a high-energy oxidant with a high specific impulse and low toxicity [3].

Research on HAN has mainly focused on the mechanism of thermal decomposition. In separate studies using mass spectrometry, Izato *et al.* [4] and Souagh *et al.* [5] commonly identified HNO_3, N_2O, and H_2O as thermal decomposition partial products of HAN, but Izato *et al.* [4] believed that the products also include N_2 and NH_3, and Souagh *et al.* [5] considered the products also include NO and NO_2. Using an infrared spectrometer, Cheng *et al.* [6] identified N_2O, NO, H_2O, and NO_2 as the thermal decomposition products of HAN. Meanwhile, the reaction pathway of HAN thermal decomposition has been investigated through quantum chemical simulations. Early studies reported various formation pathways of N_2O. For example, Oxley *et al.* [7] believed that N_2O is produced by the reaction of intermediate products HNO_2 and NH_2OH. In recent years, Izato *et al.* [4], Taylor *et al.* [8], and Zhang *et al.* [9] discovered that N_2O is produced by the reaction of intermediate products HNO and HNO. However, elucidating the electrocatalytic decomposition mechanism of HAN on electrode surfaces is essential for advancing the electrically controlled combustion mechanism of solid propellants. At present, this topic has been scantily researched

and usually focuses on electrolytic effects or product analysis. For example, Koh *et al.* [10] studied the effects of power supply and electrode materials on the electrocatalytic decomposition of HAN. They demonstrated higher performance with copper or aluminum electrodes than with carbon electrodes and reported that a power supply exceeding 100 W can effectively trigger decomposition. Sun *et al.* [11] studied the effects of electrolysis voltage and electrode surface area on the electrolysis of HAN solution. They reported an optimal voltage for electrolysis under fixed conditions. This is caused by an inhibition phenomenon at the anode, which can be alleviated by increasing the surface area of the anode electrode. Haung *et al.* [12] experimentally studied electrolysis in the HAN solution using a U-shaped bottle as the electrolytic cell container, which effectively separates the products of anode and cathode electrolysis. After electrolysis, the cathode and anode solutions became alkaline and acidic, respectively, producing NH_3 on the cathode and O_2 on the anode. Other scholars have studied the catalytic decomposition mechanisms of nitrate on electrode surfaces through quantum chemical simulations, providing useful references for studying the electrocatalytic decomposition mechanism of HAN on electrode surfaces. For example, Zhou *et al.* [13] studied the catalytic decomposition mechanism of HAN on electrode surfaces in depth. They optimized the adsorption configuration and catalytic decomposition pathway of HAN on Ir(110) surfaces. Calle-Vallejo *et al.* [14] calculated the variation trend of adsorption energy of nitrate on 20 surfaces of an Ag/Au bimetallic system. They showed that defective Ag/Au surfaces can enhance the catalytic activity of nitrate

reduction. Several researchers have also conducted computational studies on the electrocatalytic decomposition of water using quantum chemical simulations, which offer valuable insights. For instance, Ren *et al.* [15] analyzed the hydrogen evolution performance of a novel electrocatalyst, FeCoCuSx/CFF. Their results indicated that the Gibbs free energy of hydrogen adsorption at the Co sites within the CuS-Co9S8 heterostructure is close to zero. This finding suggests that the catalyst exhibits excellent hydrogen evolution performance.

To further elucidate the electrocatalytic decomposition mechanism of HAN on the electrode surface and explain the relevant experimental phenomena, this study builds upon the electrolysis experiments of HAN solution in a U-tube reported by Huang *et al.* [12]. We aim to explore the reaction pathways for the generation of NH_3 and O_2 during the electrocatalytic decomposition of HAN on the Cu (111) surface using quantum chemical simulations.

2. Materials and Methods

Small-molecule calculations were performed using the Gaussian 16 software [16]. The geometric optimization and vibration analysis of some small molecules were calculated using the B3LYP functional at the 6-31G(d) basis-set level. The B3LYP functional is commonly used and provides fast convergence with low dependence on integration lattice points. At the 6-31G(d) basis-set level, the B3LYP functional is sufficiently accurate for geometric optimization and vibration analysis [17]. The free energies of some small molecules were calculated using the coupled-cluster method with single, double, and perturbative triple excitations (CCSD(T)) method at the def2-QZVPP basis-set level. The CCSD (T) method is a high-precision quantum chemistry calculation method with sufficient accuracy at the def2-QZVPP basis-set level [18,19]. In this article, the adsorption structure of molecules on the Cu(111) surface was simulated using the CP2K software [20], which quickly calculates the periodic crystal structure of Cu metal using the density functional theory. Figure 1 is a unit cell model diagram of the Cu(111) surface, a common stable crystal plane. Panels (a) and (b) of this figure present a front and top view of the model, respectively. The adsorption structure was calculated under the Perdew–Burke–Ernzerhof functional with the DZVP–GTH pseudopotential basis set. The calculation speed was improved using the Gaussian plane wave method. The vacuum layer was set to 15 Å to avoid interactions between adjacent unit cell molecules, the plane wave cutoff energy was 600 Ry, the energy and intermolecular force convergence standards were set to 10^{-6} Hartree and 4.5×10^{-4} Hartree/Bohr, respectively, and the k-point setting was $3 \times 3 \times 1$. The Van der Waals correction was performed using the Grimme method [21]. The free energy was calculated as

$$\Delta G = \Delta E + \Delta ZPE + \Delta H_{0 \to T} - T\Delta S,$$

where ΔE and ΔZPE represent the changes in the single-point and zero-point energies, respectively, $\Delta H_{0 \to T}$ represents the enthalpy change during a temperature change from 0 K to T, and ΔS represents the entropy change.

2.1. Reaction path of electrocatalytic decomposition

Under water-solvent conditions, HAN decomposes into NH_3OH^+ and NO_3^- ions [22]. The aqueous solvent condition is simulated using the implicit solvent SMD (Solvent Model based on Density) model. The configuration changes of HAN under vacuum and water-solvent

conditions have been shown in Figure 2, and the energies were calculated using Gaussian 16 software [16]. Under vacuum and water-solvent conditions, the HAN molecule is configured as $NH_2OH \cdot HNO_3$ and $NH_3OH^+ \cdot NO_3^-$, respectively. As $NH_3OH^+ \cdot NO_3^-$ has a lower free energy of configuration than $NH_2OH \cdot HNO_3$, HAN easily decomposes into NH_3OH^+ and NO_3^- ions under water-solvent conditions. The electrocatalytic decomposition mechanism of HAN has been shown in Figure 3, where '*' represents adsorbed molecules, and radicals are identified with '·' (for example, '·OH' denotes OH radicals). Under a potential difference, anions and cations will move toward the anode (which tends to lose electrons) and cathode (which tends to gain electrons), respectively. As the NO_3^- ions move toward the anode, they lose one electron and adsorb as $*NO_3$ on the anode surface Eq. (1). Figure 4(a) shows the configuration of $*NO_3$. The two O atoms of NO_3 are adsorbed on adjacent Cu atoms at the anode surface with different bond lengths (2.040 Å and 2.045 Å) and a bond angle of 119.337° between the adsorbed O and N atoms. $*NO_3$ dissociates into $*NO_2$ and $* \cdot O$ on the anode surface Eq. (2). $*NO_2$ is configured as shown in Figure 4(b). The two O atoms of NO_2 are adsorbed on adjacent Cu atoms on the anode surface with the same bond lengths as $*NO_3$ (2.040 Å and 2.045 Å). The bond angle between the adsorbed O and N atoms is slightly smaller in $*NO_2$ than the bond angle between the adsorbed O and N atoms in $*NO_3$. Figure 4(c) shows the configuration of $* \cdot O$. The bond
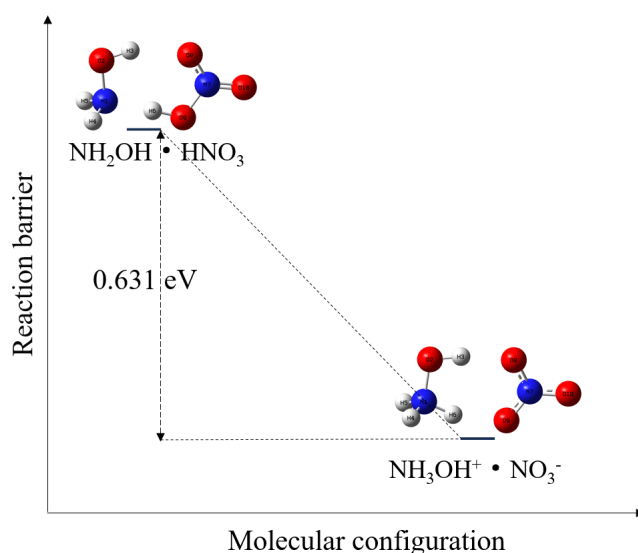
Figure 2. Configurational changes of HAN under vacuum and water-solvent conditions.

Figure 1. Unit cell model diagram of the Cu (111) surface: (a) front view; (b) top view.
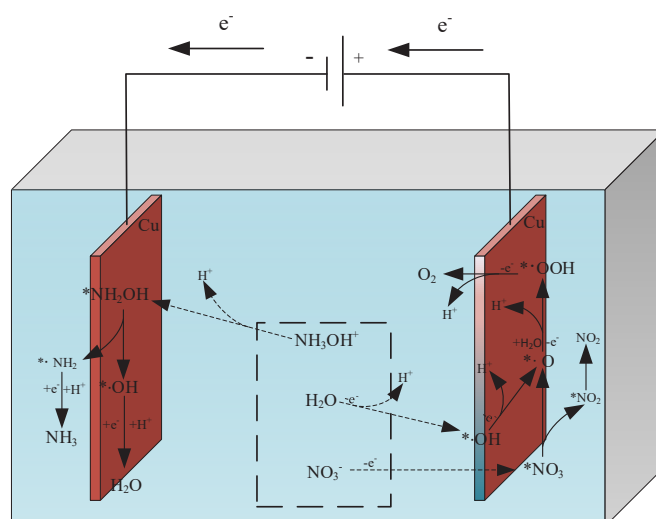
Figure 3. Diagram showing the electrocatalytic decomposition mechanism of HAN.
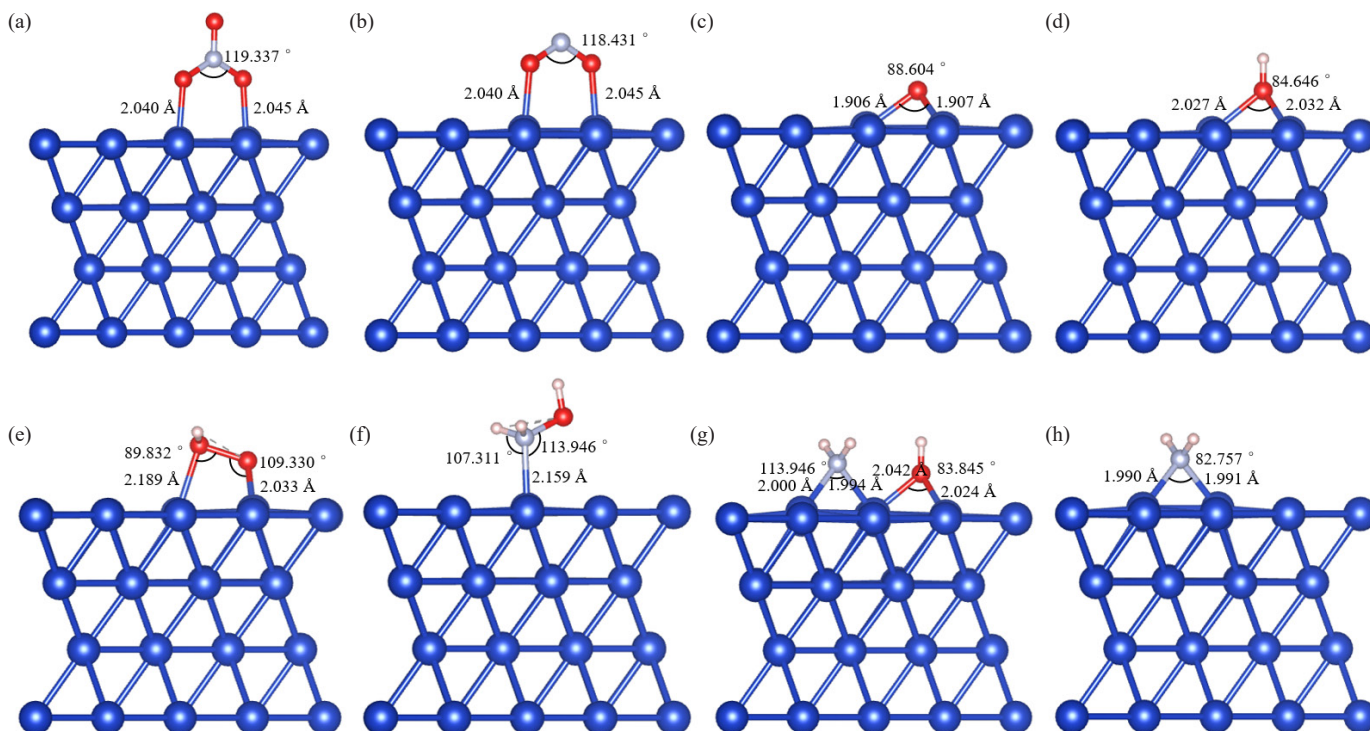
Figure 4. Configurations of the adsorbed molecules involved in electrocatalytic decomposition: (a) *NO_3; (b) *NO_2; (c) *·O; (d) *·OH; (e) *·OOH; (f) *NH_2OH; (g) *(·NH_2 + ·OH); (h) *·NH_2.

lengths between the O and adjacent Cu atoms on the anode surface are 1.906 Å and 1.907 Å, with a bond angle of 88.604°. *NO_2 can desorb from the anode surface as NO_2 see Eq. (3):

$$* + NO_3^- - e^- = *NO_3 \tag{1}$$

$$* + *NO_3 = *NO_2 + *·O \tag{2}$$

$$*NO_2 = * + NO_2 \tag{3}$$
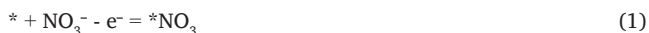
H_2O molecules lose one electron, decomposing into *·OH and H^+ ions on the anode surface Eq. (4). Figure 4(d) shows the configuration of *·OH. The bond lengths between the O atom and adjacent Cu atoms on the anode surface are 2.027 Å and 2.032 Å, with a bond angle of 84.646°. *·OH loses one electron on the anode surface, forming *·O and H^+ Eq. (5). The *·O radicals react with H_2O molecules, losing one electron to form H^+ and *·OOH Eq. (6). Figure 4(e) shows the configuration of *·OOH. The two O atoms of ·OOH are adsorbed on adjacent Cu atoms on the anode surface with bond lengths of 2.189 Å and 2.033 Å and bond angles of 89.832° and 109.330°, respectively. *·OOH loses one electron on the anode surface, forming H^+ and O_2 Eq. (7). The reaction equations are as follows:

$$* + H_2O - e^- = *·OH + H^+ \tag{4}$$

$$*·OH - e^- = *·O + H^+ \tag{5}$$

$$*·O + H_2O - e^- = *·OOH + H^+ \tag{6}$$

$$*·OOH - e^- = * + ·O_2 + H^+ \tag{7}$$
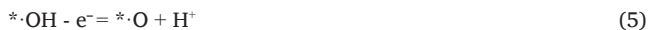
Under the action of the potential difference, NH_3OH^+ ions move toward the cathode, where they dissociate into *NH_2OH and H^+ ions on the cathode surface Eq. (8). Figure 4(f) shows the configuration of *NH_2OH. The N atom of NH_2OH adsorbs with a bond length of 2.159 Å near the Cu atom on the cathode surface. The bond angles are 107.311° between the Cu, N, and H atoms and 113.946° between the Cu, N, and O atoms. *NH_2OH dissociates into *(·NH_2 + OH) Eq. (9) with the configuration shown in Figure 4(g). The bond lengths between the N atom of ·NH_2 and the two adjacent Cu atoms on the cathode surface are 2.000 Å and 1.994 Å with a bond angle of 113.946°. Meanwhile, the bond lengths between the O atom of ·OH and the two adjacent Cu atoms on the cathode surface are 2.042 Å and 2.024 Å, with a bond angle of 83.845°. *·NH_2 obtains an electron at the cathode and

combines with H^+ ions to form NH_3 Eq. (10). Figure 4(h) shows the configuration of NH_2. The N atom of ·NH_2 bonds with two adjacent Cu atoms on the cathode surface with bond lengths of 1.990 Å and 1.991 Å and a bond angle of 82.757°. *·OH obtains an electron at the cathode and combines with H^+ ions to form H_2O Eq. (11). The reaction equations are as follows:

$$* + NH_3OH^+ = *NH_2OH + H^+ \tag{8}$$

$$*NH_2OH = *(·NH_2 + ·OH) \tag{9}$$

$$*·NH_2 + H^+ + e^- = * + NH_3 \tag{10}$$

$$*·OH + H^+ + e^- = * + H_2O \tag{11}$$

3. Results and Discussion

3.1. Anodic reaction mechanism

Table 1 lists the thermodynamic parameters of the relevant molecules during the anodic reaction process, calculated using CP2K software. As analyzed in the previous section, NO_3^- ions near the anode first lose one electron and adsorb to the anode surface. To avoid the CP2K calculation of the free energy of NO_3^- ions, the formation free energy of Eq. (1) was obtained by summing the formation free energies of Eqs. (12), (13), and (14); that is, $\Delta G_1 = \Delta G_{12} + \Delta G_{13} + \Delta G_{14}$, where ΔG represents the formation free energy and the subscript denotes the number of the reaction equation. In this expression, $\Delta G_{12} = G(*NO_3) + 0.5G(H_2(g)) - G(HNO_3(g)) - G(*)$, where G represents the free energy and $H^+ + e^-$ is replaced by half the free energy of H_2. According to Calle-Vallejo et al. [14], $\Delta G_{13} = 0.317$ eV and $\Delta G_{14} = 0.075$ eV. As only the vibrations of adsorbed molecules are relevant, the surface free energy of the anode is replaced by the single-point energy [23]. From the data in Table 1, ΔG_1 was determined as 0.001 eV. Eqs. (12)–(14) are computed as

$$* + HNO_3(g) - e^- = *NO_3 + H^+ \tag{12}$$

$$NO_3^- + H^+ = HNO_3(l) \tag{13}$$

$$HNO_3(l) = HNO_3(g) \tag{14}$$

Table 1. Thermodynamic parameters of the molecules involved in the anodic reaction process.

Molecular formula	E_{ele} (Hartree)	T (K)	ZPE (Hartree)	ΔG (Hartree)	G (Hartree)
*	−3080.168	——	——	——	——
*NO₃	−3138.089	298.15	0.016	0.012	−3138.077
HNO₃(g)	−58.494	298.15	0.025	0.017	−58.477
H₂(g)	−1.162	298.15	0.012	−0.002	−1.164
*NO₂	−3122.099	298.15	0.011	0.008	−3122.091
*·O	−3096.186	298.15	0.003	0.003	−3096.183
NO₂(g)	−41.881	298.15	0.009	−0.017	−41.897
O₂(g)	−31.928	298.15	0.004	−0.002	−31.931
H₂O(l)	−17.220	298.15	——	0.000	−17.220
*·OH	−3096.806	298.15	0.013	0.012	−3096.794
*·OOH	−3112.733	298.15	0.017	0.015	−3112.718

Note: *: anodic surface; E_{ele}: Single-point energy; T: Temperature; ZPE: Zero-point energy; ΔG: Free energy correction: G: Represents free energy.

The formation free energy of *NO₃ dissociation into *NO₂ and *·O on the anode surface can be expressed as $\Delta G_2 = G(*NO_2) + G(*\cdot O) - G(*NO_3) - G(*)$. From the data in Table 1, ΔG_2 was obtained as −0.811 eV. Given the formation free energy of NO₂ on the anode surface $\Delta G_3 = G(*) + G(NO_2(g)) - G(*NO_2)$ and the data in Table 1, ΔG_3 was obtained as 1.125 eV. The formation free energy of H₂O molecules decomposing into *·OH and H⁺ ions on the anode surface can be expressed as $\Delta G_4 = G(*\cdot OH) + 0.5G(H_2(g)) - G(H_2O(l)) - G(*)$, giving $\Delta G_4 = 0.310$ eV based on the data in Table 1. The free energy of *·O and H⁺ formation on the anode surface after *·OH adsorption is computed as $\Delta G_5 = G(*\cdot O) + 0.5G(H_2(g)) - G(*\cdot OH)$, from which $\Delta G_5 = 0.782$ eV from the data in Table 1. The formation free energy of H⁺ and *·OOH formed by the reaction between *·O and H₂O molecules is $\Delta G_6 = G(*\cdot OOH) + 0.5G(H_2(g)) - G(*\cdot O) - G(H_2O(l))$. From the data in Table 1, ΔG_6 was obtained as 2.799 eV. Finally, the formation free energy of H⁺ and O₂ on the anode surface of *·OOH, given by $\Delta G_7 = G(*) + G(O_2(g)) + 0.5G(H_2(g)) - G(*\cdot O) - G(H_2O(l))$, was obtained as $\Delta G_7 = 1.028$ eV using the data of Table 1.

From the above analysis, it was concluded that O₂ on the anode surface can be formed through two pathways: electrocatalytic decomposition of NO₃⁻ ions and electrocatalytic decomposition of H₂O molecules. Figure 5 shows the potential barrier diagram of NO₃⁻ ion decomposition on the anode surface. The potential barrier of electron adsorption of NO₃⁻ ions is almost 0, and that of *NO₃ decomposition into *NO₂ and *·O is negative, indicating the process can easily spontaneously occur. Meanwhile, NO₂ desorption, *·O to *·OOH conversion, and *·OOH to O₂ conversion must cross potential barriers of 1.125, 2.799, and 1.028 eV, respectively. Figure 6 shows the potential barrier diagram of H₂O decomposition on the anode surface. The conversion of adsorbed H₂O molecules to *·OH, conversion of *·OH to
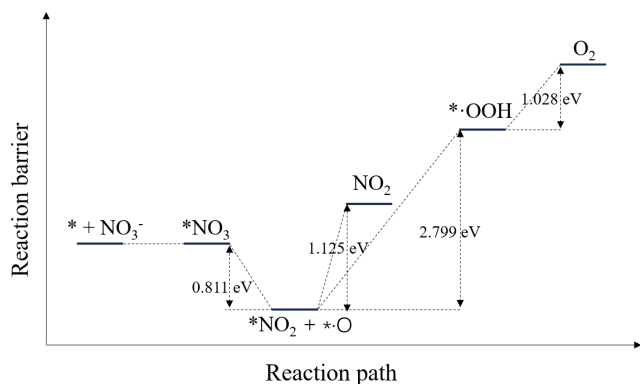
Figure 5. Reaction barrier diagram of NO₃⁻ ion decomposition on the anode surface.
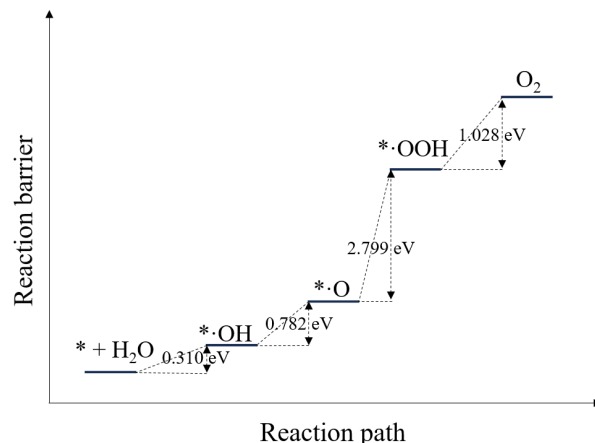
Figure 6. Reaction barrier diagram of H₂O molecule decomposition on the anode surface.

*·O, and subsequent conversion to *·OOH and O₂, like NO₃⁻ ions, must cross potential barriers of 0.310 eV, 0.782 eV. As NO₃⁻ conversion to O₂ has a lower potential barrier than H₂O conversion to O₂ on the anode surface, the decomposition rate of NO₃⁻ exceeds that of H₂O, and NO₃⁻ decomposition is the main pathway of O₂ generation at the anode.

3.2. Cathodic reaction mechanism

Table 2 lists the thermodynamic parameters of the molecules involved in the cathodic reaction process, calculated using CP2K software. As analyzed in the previous subsection, NH₃OH⁺ ions first dissociate into *NH₂OH and H⁺ ions on the cathode surface. To avoid the CP2K calculation of the free energy of NH₃OH⁺ ions, the formation free energy of the acid-dissociation reaction of NH₃OH⁺ ions Eq. (15) was first calculated using Gaussian software. Next, the formation free energy of Eq. (16) was calculated in CP2K software to obtain the formation free energy of Eq. (8), namely, $\Delta G_8 = \Delta G_{15} + \Delta G_{16}$, where the formation free energy of Eq. (15) was calculated as $\Delta G_{15} = 0.349$ eV and that of Eq. (16) was obtained as $\Delta G_{16} = G(*NH_2OH) - G(NH_2OH) - G(*)$ = 0.310 eV using the data in Table 2. Therefore, G_8 was obtained as 0.279 eV. The formation free energy of NH₂OH dissociation into *(·NH₂ + ·OH) is $\Delta G_9 = G(*(\cdot NH_2 + \cdot OH)) - G(*NH_2OH)$. From the data in Table 2, ΔG_9 was obtained as −1.954 eV. The reaction equations are given by

$$NH_3OH^+ = NH_2OH + H^+ \tag{15}$$

$$* + NH_2OH = *NH_2OH \tag{16}$$

Table 2. Thermodynamic parameters of the molecules involved in the cathodic reaction process.

Molecular formula	E_{ele} (Hartree)	T (K)	ZPE (Hartree)	ΔG (Hartree)	G (Hartree)
*	−3080.168	——	——	——	——
*NH₂OH	−3107.887	298.15	0.041	0.039	−3107.848
NH₂OH	−27.692	298.15	0.039	0.014	−27.678
H₂(g)	−1.162	298.15	0.012	−0.002	−1.164
*(·NH₂ + ·OH)	−3107.956	298.15	0.038	0.036	−3107.920
*·NH₂	−3091.318	298.15	0.025	0.023	−3091.295
H₂O(l)	−17.220	298.15	——	0.000	−17.220
NH₃	−11.738	298.15	0.034	0.014	−11.723
*·OH	−3096.806	298.15	0.013	0.012	−3096.794
*·OOH	−3112.733	298.15	0.017	0.015	−3112.718

Note: *: cathode surface; E_{ele}: Single-point energy; T: Temperature; ZPE: Zero-point energy; ΔG: Free energy correction: G: Represents free energy
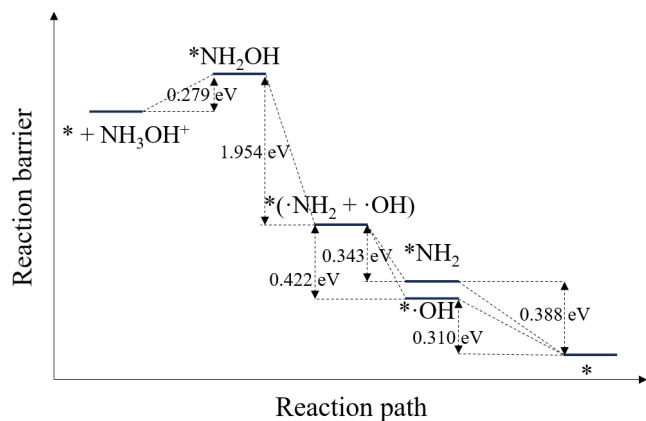
Figure 7. Reaction barrier diagram of NH_3OH^+ ion decomposition on the cathode surface.

$*(\cdot NH_2 + \cdot OH)$ reacts with H^+ ions to remove an H_2O molecule Eq. (17). Next, $*\cdot NH_2$ and H^+ ions combine to form NH_3 Eq. (17) with a formation free energy of $\Delta G_{17} = G(*\cdot NH_2) + G(H_2O(l)) - G(*(\cdot NH_2 + \cdot OH)) - 0.5G(H_2(g))$. From the data in Table 2, ΔG_{17} was obtained as -0.343 eV. Meanwhile, the formation free energy of Eq. (10) is $\Delta G_{10} = G(*) + G(NH_3) - G(*\cdot NH_2) - 0.5G(H_2(g)) = -0.388$ eV using the data in Table 2. $*(\cdot NH_2 + \cdot OH)$ reacts with H^+ ions to remove an NH_3 molecule Eq. (18). The $*\cdot OH$ and H^+ ions then combine to form H_2O with a formation free energy of $\Delta G_{18} = G(\cdot OH) + G(NH_3) - G(*(\cdot NH_2 + \cdot OH)) - 0.5G(H_2(g))$. From the data in Table 2, ΔG_{18} was obtained as -0.422 eV. The formation free energy of Eq. (11) is $\Delta G_{11} = G(*) + G(H_2O(l)) - G(*\cdot OH) - 0.5G(H_2(g))$. From the data in Table 2, ΔG_{11} was determined as -0.310 eV. The reaction equations are as follows:

$$*(\cdot NH_2 + \cdot OH) + H^+ + e^- = *\cdot NH_2 + H_2O(l) \tag{17}$$

$$*(\cdot NH_2 + \cdot OH) + H^+ + e^- = *\cdot OH + NH_3 \tag{18}$$
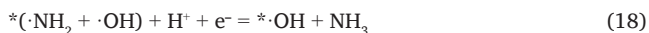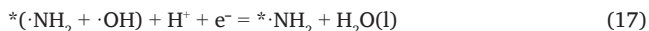
As shown in the above analysis, NH_3OH^+ ions gradually decompose on the cathode surface. Figure 7 shows the reaction potential-barrier diagram of NH_3OH^+ decomposition on the cathode surface. The potential barrier of electron adsorption by NH_3OH^+ ions and subsequent $*NH_2OH$ decomposition is 0.279 eV. As the energy increases during conversion, the reaction cannot easily proceed spontaneously. However, when $*NH_2OH$ decomposes into $*(NH_2 + OH)$, the energy barrier is lowered and this reaction can spontaneously proceed. The energy also decreases when $*(\cdot NH_2 + \cdot OH)$ converts to $*NH_2$ and $*\cdot OH$, but the larger decrease in energy during conversion to $*\cdot OH$ indicates a faster reaction rate of conversion to $*\cdot OH$ than of conversion to $*NH_2$. Finally, the desorption of adsorbed molecules $\cdot NH_2$ and $\cdot OH$ from the cathode surface can also spontaneously proceed. Therefore, the decisive step in NH_3OH^+ decomposition is electron adsorption and decomposition of NH_3OH^+ ions to $*NH_2OH$. All subsequent decomposition processes can spontaneously occur.

4. Conclusions

The main conclusions of the study are summarized below.

(1) Under water-solvent conditions, HAN easily decomposes into NH_3OH^+ and NO_3^- ions. Under the action of a potential difference, NH_3OH^+ ions and NO_3^- ions move toward the cathode and anode, respectively, where they undergo electrocatalytic decomposition reactions. Specifically, NH_3OH^+ ions decompose into NH_3 and H_2O on the cathode surface, and NO_3^- ions decompose into NO_2 and O_2 on the anode surface.

(2) O_2 at the anode surface can be generated via two pathways: the electrocatalytic decomposition of NO_3^- ions and the electrocatalytic decomposition of H_2O molecules on the anode surface. The key difference between these two pathways lies in the formation of the

$*\cdot O$ intermediate. For NO_3^- ions, the energy decreases during the formation of $*\cdot O$, with a reaction barrier of -0.811 eV, indicating that the reaction is highly spontaneous. In contrast, for H_2O molecules, the energy increases during the formation of $*\cdot O$, with a reaction barrier of +0.782 eV. This suggests that the formation of $*\cdot O$ from H_2O is more challenging. Therefore, the electrocatalytic decomposition of NO_3^- ions on the anode surface are the dominant pathway for O_2 generation at the anode.

(3) The cathodic surface reaction easily occurs, and its rate-determining step is the electron adsorption and decomposition of NH_3OH^+ ions to form $*NH_2OH$. The energies of all subsequent decomposition processes decrease, indicating that the reaction occurs spontaneously. On the cathodic surface, $*(\cdot NH_2 + OH)$ conversion to $*\cdot NH_2$ competes with $*(NH_2 + \cdot OH)$ conversion to $*\cdot OH$. The greater energy decrease during conversion to $*\cdot OH$ indicates a higher reaction rate of $*\cdot OH$ formation than of $*\cdot NH_2$ formation from $*(NH_2 + \cdot OH)$.

(4) During the anodic reaction, several processes generate hydrogen ions (H^+), while at the cathode, multiple reactions consume hydrogen ions. This leads to the cathodic solution becoming alkaline and the anodic solution becoming acidic after the electrocatalytic decomposition of the HAN solution.

(5) The electrocatalytic decomposition mechanism of HAN on the Cu(111) surface is highly complex. This study primarily analyzes the main pathways for the formation of O_2 and NH_3. Future research could utilize quantum chemical simulations to predict potential by-products, thereby guiding experimental investigations. Additionally, deeper insights into the reaction mechanism could be revealed through atomic charge calculations and orbital composition analysis.

CRediT authorship contribution statement

Men Li and Tianpeng Li: Conceptualization, **Men Li:** Methodology, **Men Li, Tianpeng Li and Xinbao Gao**: Validation, **Men Li:** Data Curation, **Men Li:** Writing – Original Draft Preparation, **Men Li, Tianpeng Li, Yin Huang and Xinbao Gao:** Writing – Review & Editing.

Declaration of competing interest

All authors disclose no conflicts of interest.

Declaration of Generative AI and AI-assisted technologies in the writing process

The authors confirm that there was no use of artificial intelligence (AI)-assisted technology for assisting in the writing or editing of the manuscript and no images were manipulated using AI.

Acknowledgement

References

1. Xia, X., Fu, X.L., Hu, S., Zhao, Y., 2024. Research progress of new electrically controlled solid propellants for smart ammunition. *Chinese Journal of Explosives & Propellants*, **47**, 287-304. https://doi.org/10.14077/j.issn.1007-7812.202306019.
2. Li, M., Li, T.P., Gao, X.B., 2024. Research progress in ECSP preparation and electronically controlled combustion technology. Journal *of Solid Rocket Technology*, **47**, 155–163. https://doi.org/10.7673/j.issn.1006-2793.2024.02.002.
3. Chai, W.S., Cheah, K.H., Wu, M.-H., Koh, K.S., Sun, D., Meng, H., 2022. A review on hydroxylammonium nitrate (HAN) decomposition techniques for propulsion application. *Acta Astronautica*, **196**, 194-214. https://doi.org/10.1016/j.actaastro.2022.04.011
4. Izato, Y.-ichiro, Koshi, M., Miyake, A., 2017. Decomposition pathways for aqueous hydroxylammonium nitrate solutions: A DFT study. *Central European Journal of Energetic Materials*, **14**, 888-916. https://doi.org/10.22211/cejem/71193
5. Souagh, A., Remissa, I., Atamanov, M., El Alaoui, H., Amrousse, R., 2022. Comparative study of the thermal decomposition of hydroxylammonium nitrate green energetic compound: Combination between experimental and DFT calculation. *International Journal of Energetic Materials and Chemical Propulsion*, **21**, 31-8. https://doi.org/10.1615/intjenergeticmaterialschemprop.2022044056

6. Cheng, H.B., Wang, Z., Tao, B.W., Huang, Y., Wu, Z., Li, X.W., 2018. Study on thermal decomposition characteristics of hydroxylammonium nitrate and its stabilization technology. *Chemical Propellants & Polymeric Materials*, 2018;16:80-5. https://doi.org/10.16572/j.issn1672-2191.201809027.

7. Oxley, J.C., Brower. K.R., 1988. Thermal decomposition of hydroxylamine nitrate. *Propulsion* **872**, 63–70. https://doi.org/10.1117/12.943754.

8. Taylor, N.R., Brummel, M.H., Mooney, M.M., Kerber, T.V., Lemmer, K.M., 2024. On the formation of ammonia from the thermal decomposition of hydroxylammonium nitrate vapor. *Journal of Ionic Liquids*, **4**, 100083. https://doi.org/10.1016/j.jil.2024.100083

9. Zhang, K., Thynell, S.T., 2018. Thermal decomposition mechanism of aqueous hydroxylammonium nitrate (HAN): Molecular simulation and kinetic modeling. *The Journal of Physical Chemistry. A*, **122**, 8086-8100. https://doi.org/10.1021/acs.jpca.8b05351

10. Koh, K.S., Chin, J., Wahida Ku Chik, T.F., 2013. Role of electrodes in ambient electrolytic decomposition of hydroxylammonium nitrate (HAN) solutions. *Propulsion and Power Research*, **2**, 194-200. https://doi.org/10.1016/j.jppr.2013.07.002

11. Sun, D., Dai, Q., Chai, W.S., Fang, W., Meng, H., 2022. Experimental studies on parametric effects and reaction mechanisms in electrolytic decomposition and ignition of HAN solutions. *ACS Omega*, **7**, 18521-18530. https://doi.org/10.1021/acsomega.2c01183

12. Huang Y, Zhang XP, Pang AM, Li HX, Wang Y, Cheng HB. Research progress on new intelligent electronic control solid propellant technology. In The 40th Technical Exchange Conference and the 4th Aerospace Power Joint Conference of China Aerospace Third Professional Information Network, 2024.

13. Zhou, X., Wang, Q., Shi, Z., Hu, X., Yao, T., Huang, Y., 2023. A theoretical investigation of the catalytic decomposition of hydroxylamine nitrate on ir(1 1 0) surface. *Computational and Theoretical Chemistry*, **1225**, 114141. https://doi.org/10.1016/j.comptc.2023.114141

14. Calle-Vallejo, F., Huang, M., Henry, J.B., Koper, M.T., Bandarenka, A.S., 2013. Theoretical design and experimental implementation of Ag/Au electrodes for the electrochemical reduction of nitrate. *Physical Chemistry Chemical Physics: PCCP*, **15**, 3196-3202. https://doi.org/10.1039/c2cp44620k

15. Ren, R., Wang, Y., Li, T., 2025. In situ growth of feCo sulfides on cobalt iron foam for efficient high-current-density hydrogen evolution reaction electrocatalysis. *Journal of Colloid and Interface Science*, **682**, 288-297. https://doi.org/10.1016/j.jcis.2024.11.251

16. Frisch, M.J., Trucks, G.W., Schlegel, H.B., Scuseria, G.E., Robb, M.A., Cheeseman, J.R., Scalmani, G., Barone, V., Petersson, G. A., Nakatsuji, H., Li, X, Caricato, M., Marenich, A.V., Bloino, J., Janesko, B.G., Gomperts, R., Mennucci, B., Hratchian, H.P., Ortiz, J.V., Izmaylov, A.F., Sonnenberg, J.L., Williams-Young, D., Ding, F., Lipparini, F., Egidi, F., Goings, J., Peng, B., Petrone, A., Henderson, T., Ranasinghe, D., Zakrzewski, V.G., Gao, J., Rega, N., Zheng, G., Liang, W., Hada, M., Ehara, M., Toyota, K., Fukuda, R., Hasegawa, J., Ishida, M., Nakajima, T., Honda, Y., Kitao, O., Nakai, H., Vreven, T., Throssell, K., Montgomery, J.A., Jr., Peralta, J.E., Ogliaro, F., Bearpark, M.J., Heyd, J.J., Brothers, E.N., Kudin, K.N., Staroverov, V.N., Keith, T.A., Kobayashi, R., Normand, J., Raghavachari, K., Rendell, A.P., Burant, J.C., Iyengar, S.S., Tomasi, J., Cossi, M., Millam, J.M., Klene, M., Adamo, C., Cammi, R., Ochterski, J.W., Martin, R.L., Morokuma, K., Farkas, O., Foresman, J.B., Fox, D.J., 2016. Gaussian 16, Revision A.03; Gaussian, Inc.: Wallingford CT.

17. Liu, H., Fu, Z., Zhao, Y., Li, J., Li, S., Pi, Z., 2024. Study of lubrication adsorption behavior based on molecular dynamics simulation. *Equipment Environmental Engineering* **2024**, 28–36. https://doi.org/10.2139/ssrn.4879964.

18. Donchev, A.G., Taube, A.G., Decolvenaere, E., Hargus, C., McGibbon, R.T., Law, K.H., Gregersen, B.A., Li, J.L., Palmo, K., Siva, K., Bergdorf, M., Klepeis, J.L., Shaw, D.E., 2021. Quantum chemical benchmark databases of gold-standard dimer interaction energies. *Scientific Data*, **8**, 55. https://doi.org/10.1038/s41597-021-00833-x

19. Yu, Y., Pan, L., Sun, Q., Wang, J., 2024. The mechanism and kinetics of the atmospheric oxidation of $CF_3(CF_2)_2CH = CH_2$ (HFC-1447fz) by hydroxyl radicals: *ab initio* investigation. *Physical Chemistry Chemical Physics*, **26**, 10989-10997. https://doi.org/10.1039/d3cp06149c

20. Kühne, T.D., Iannuzzi, M., Del Ben, M., Rybkin, V.V., Seewald, P., Stein, F., Laino, T., Khaliullin, R.Z., Schütt, O., Schiffmann, F., Golze, D., Wilhelm, J., Chulkov, S., Bani-Hashemian, M.H., Weber, V.éry, Borštnik, U., Taillefumier, M., Jakobovits, A.S., Lazzaro, A., Pabst, H., Müller, T., Schade, R., Guidon, M., Andermatt, S., Holmberg, N., Schenter, G.K., Hehn, A., Bussy, A., Belleflamme, F., Tabacchi, G., Glöß, A., Lass, M., Bethune, I., Mundy, C.J., Plessl, C., Watkins, M., VandeVondele, J., Krack, M., Hutter, J.ürg, 2020. CP2K: An electronic structure and molecular dynamics software package - quickstep: Efficient and accurate electronic structure calculations. *The Journal of Chemical Physics*, **152**, 194103. https://doi.org/10.1063/5.0007045

21. Grimme, S., Antony, J., Ehrlich, S., Krieg, H., 2010. A consistent and accurate ab initio parametrization of density functional dispersion correction (DFT-d) for the 94 elements H-Pu. *The Journal of Chemical Physics*, **132**, 154104. https://doi.org/10.1063/1.3382344

22. Broemmelsiek, E.J., Rovey, J.L., Berg, S.P., 2021. Effect of metal sequestrants on the decomposition of hydroxylammonium nitrate. *Catalysts*, **11**, 1488. https://doi.org/10.3390/catal11121488

23. Nørskov, J.K., Rossmeisl, J., Logadottir, A., Lindqvist, L., Kitchin, J.R., Bligaard, T., Jónsson, H., 2004. Origin of the overpotential for oxygen reduction at a fuel-cell cathode. *The Journal of Physical Chemistry. B*, **108**, 17886-17892. https://doi.org/10.1021/jp047349j